Title
Decomposition of the Toxic Nerve Agent Sarin on Oxygen Vacancy Sites of Rutile TiO2(110)

Journal
The Journal of Physical Chemistry C, 127(17)

ISSN
1932-7447

Authors
Tesvara, Celine
Karwacki, Christopher J
Sautet, Philippe

Publication Date
2023-05-04

DOI
10.1021/acs.jpcc.2c08525

Decomposition of the Toxic Nerve Agent Sarin on Oxygen Vacancy Sites of Rutile TiO_2(110)

Celine Tesvara[a], Christopher J. Karwacki[b], Philippe Sautet[a,c*]

[a] Chemical and Biomolecular Engineering Department, University of California, Los Angeles, Los Angeles, CA 90095, USA

[b] DEVCOM Chemical Biological Center, Aberdeen Proving Ground, Maryland 21010-5424, USA

[c] Chemistry and Biochemistry Department, University of California, Los Angeles, Los Angeles, CA 90095, USA

Corresponding Author: sautet@ucla.edu

Abstract

To design effective personal protective equipment against chemical attacks, the understanding of chemical warfare agents (CWAs) decomposition chemistry is crucial. Metal oxides, particularly TiO_2 have been found to be promising materials to trap and decompose CWAs. This work explores the possible decomposition pathways of sarin on a model rutile TiO_2(110) surface with and without the presence of surface oxygen vacancies. Sarin adsorbs on the surface mainly by its P=O unit via a dative P=O-Ti_{5c} bond, similar to its simulant dimethyl methylphosphonate (DMMP). Sarin decomposition on the pristine surface is possible at 455 K, and proceeds via O-C bond cleavage, with a barrier of 1.17 eV, resulting in the production of surface-bonded monofluorophosphate and isopropoxy, while P-OR (R= C_3H_7 isopropyl) or P-F cleavage is highly activated with barriers larger than 2 eV. However, the production of gas-phase propene after O-C cleavage has a high activation barrier (1.6 eV). In the presence of O vacancies, the barriers to cleave the P-F and P-OR bonds are greatly reduced and these cleavages become possible

at a moderate temperature (425 K). In comparison to its simulant DMMP, the decomposition of sarin proceeds faster on the oxygen vacancy as the cleavage of the P-F bond is more facile and the binding of F on surface Ti creates a thermodynamically stable intermediate. The electronic effects of the F ligand also facilitate the P-OR bond cleavage at the O vacancy site. Frequency calculations validate the energy pathways: intact molecular adsorption of sarin can explain the experimental spectrum at room temperature, while further decomposition by C-O or P-F bond cleavage, presumably on the pristine surface and at O vacancies respectively, are responsible for the spectral evolution seen at 500K, in agreement with calculated barriers.

Introduction

One of the most used and dangerous chemical warfare agents (CWAs) is the nerve gas agent sarin (commonly referred to as GB), with its prevalent use dating back from the first world war, and more recently for terrorist attacks.[1] However there is a lack of understanding of the molecular interaction and decomposition mechanisms of sarin on different types of materials, which poses a critical challenge in practical applications toward the neutralization of CWAs.

Metal oxides are often the customary material chosen as the base material for protective equipment as they are efficient in trapping pollutants, present high surface areas, and are chemically stable.[2–4] The ideal metal oxide should be able to strongly adsorb CWAs and simultaneously decompose CWAs under ambient conditions, transforming them into benign compounds. To understand the interaction of such CWAs with oxide surfaces, most experimental studies substitute CWAs with simulants. Accordingly, experimental studies regarding sarin on metal oxides often replace sarin with dimethyl methylphosphonate (DMMP). The basis of this choice lies in the similarities of chemical structures between sarin and DMMP (Fig. 1). It is unclear however if DMMP is a good simulant of sarin for the decomposition chemistry at oxide surfaces.

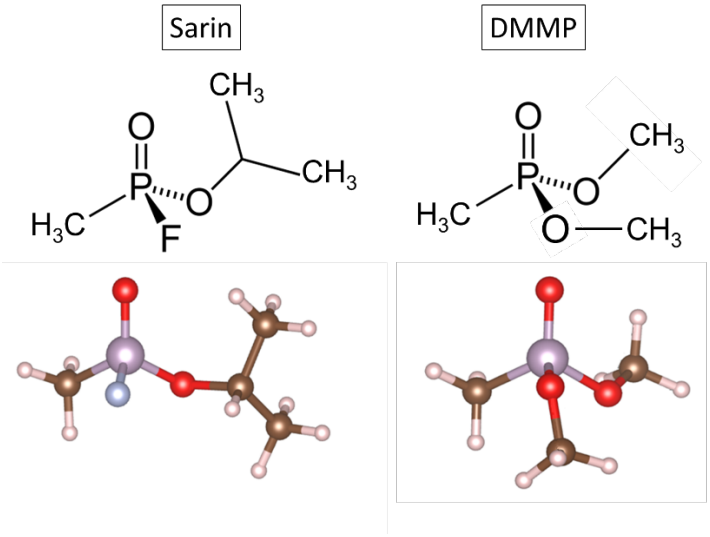

Figure 1: The chemical structures of sarin and its simulant DMMP (P: light grey, C: dark grey, O: red, F: blue, H: white)

Past works have shown that the decomposition of DMMP is indeed sensitive to the type of metal oxide used, and the presence of defects and contaminants. FTIR studies showed that aluminum oxide, magnesium, and lanthanum oxides are able to cleave the P-OCH_3 bond of DMMP at room temperature, and in the case of Fe_2O_3, Fe_3O_4, and CeO_2 activation of the P-CH_3 bond to produce dimethyl ether are also observed.[5–10] In the case of ceria, the formation of product (methanol and formaldehyde) can only be seen above 575K, signaling decomposition via P-OCH_3 between 300 to 550K.[6] On the other hand, combined experimental and theoretical studies showed that in the case of rutile-phased oxides in ultra-high vacuum conditions such as SnO_2 and TiO_2, the decomposition of DMMP via P-OCH_3 bond cleavage have considerably high barriers, and thus decomposition may be initiated via O-CH_3 bond cleavage instead.[11,12] Similar phenomenon occurs for the decomposition of another sarin surrogate, diisopropyl methylphosphonate, on alumina. Ab Initio Molecular Dynamics predicted that decomposition via the O-C bond cleavage would lead to a release of propene at high temperatures (700-1000 K).[13] Experimental studies combining X-ray photoelectron spectroscopy and temperature-programmed desorption of DMMP decomposition on rutile TiO_2 (110) under ultra-high vacuum show a broad signal for intact DMMP desorption and suggest low reactivity of TiO_2 up to 550 K.[14]

Defects, such as oxygen vacancies or hydroxyls are known to modify DMMP decomposition pathways. FTIR studies on powder titania showed that the P-OCH_3 bond cleavage is facilitated by the presence of surface hydroxyls at temperatures starting from 214 K.[15] This is denoted by

the shift of the P-CH_3 signal and a decrease of the surface O-H signal, and leads to the formation of adsorbed methyl phosphonic acid and possibly to the release of methanol.[15–18] This is similar to the behavior of DMMP observed on ZnO, zirconium hydroxide, and Zr-based metal-organic frameworks (MOFs) where DMMP is transformed into penta-coordinated phosphor-center intermediate by surface hydroxyl groups prior to the release of methanol at room temperature.[19–23] Our previous work on rutile TiO_2(110) also showed the effect of oxygen vacancies in facilitating the P-OCH_3 bond cleavage, reducing its barrier from >2 eV to 1.4 eV and rendering the process possible at 600K. It was also found that the product formation (methanol and formaldehyde) could only result from a methoxy disproportionation reaction resulting from decomposed DMMP on defect sites.[11] The influence of defects and different surface morphology on the decomposition of DIMP has been observed as well. On alumina, the release of 2-propanol is observed, however on silica, the release of propene was observed instead.[24] To move from model molecules to real toxic nerve agents, it is important to also investigate if the reactivity of sarin with TiO_2 surfaces is similar to that of the simulant DMMP and whether a similar influence of oxide surface defects can take place with sarin decomposition chemistry.

Experimental studies on sarin are rare, but the decomposition chemistry of sarin has been the subject of theoretical investigations. Cluster studies on MgO showed that the cleavage of the P-F bond has a barrier of 0.95 eV and that the fluorine ion stayed on the cluster. However, the presence of surface hydroxyl groups may reduce the barrier to 0.43 eV, resulting in the release of HF.[25] A combined XPS and DFT work on MoO_2(110) showed that the decomposition of sarin most likely proceeds via the elimination of propene, with surprisingly low barriers around 54 kJ/mol, in contrast to the case of DMMP where the lowest barrier is calculated to 116 kJ/mol on the same surface.[26] Another work on ZnO hints at the possibility of different decomposition reactivity between sarin and DMMP as the barrier to cleave the P-OR bond of DMMP on ZnO was found to be 1.77 eV, 0.6 eV higher than the barrier to cleave the P-F bond of sarin on pristine ZnO, which is 1.17 eV.[19,27] On titania, a thermodynamic study by Quintero et al. showed that sarin adsorption is dissociative by transferring F towards the surface Ti cation, which would be analogous to DMMP's P-OCH_3 bond cleavage.[28] Reaction barriers were not calculated. However, a recent work using combined IR and DFT studies on UHV-dry rutile TiO_2(110) suggested that the first step of sarin decomposition most likely proceeds via propene elimination via O-C_3H_7 bond cleavages, with a barrier of 108 kJ/mol.[29] A similar behavior is not observed,

however in the experimental study using FTIR of partially hydrated surface performed in the dark by Hirakawa et.al., where production of isopropyl methyl phosphonic acid (IMPA) is shown along with changes in OH bands linked with the displacement of OH groups, suggesting P-F bond cleavage instead.[30] On alumina, both processes (propene formation and P-F bond cleavage) are deemed to be possible; the experimental IR work of Kuiper et.al. suggests two decomposition channels of sarin, via a P-F bond cleavage or the dealkylation to produce propene.[31] To the best of our knowledge, past theoretical studies on titania have been focused only on the thermodynamic analysis or on the barrier for the first dissociation step and did not investigate further reaction steps nor studied the effect of oxygen vacancy.

Finally, despite the fact that DMMP is structurally similar to sarin, it is still now an open question whether DMMP can accurately depict the decomposition chemistry of sarin due to the difference in chemical groups (methoxy on DMMP vs -F and $-OC_3H_7$ on sarin). Thus, in this study, we will focus on investigating the decomposition pathways of sarin on rutile TiO_2(110) from quantum chemical calculations and compare these pathways with our previous work on DMMP decomposition on the same surface.[11] TiO_2 was chosen as it has been suggested as a promising material to quickly adsorb toxic agents and their degradation products. This can be seen by the strong adsorption energies of DMMP on dry rutile TiO_2(110), found in previous works.[28,32–36] Our work here aims not only to provide full and detailed decomposition studies of sarin on titanium oxide but also to serve as a benchmark comparison of the difference between sarin and DMMP decomposition on titania. Additionally, we will also investigate the effect of surface oxygen vacancy on the sarin decomposition pathways, in comparison with DMMP, and link our computational results with vibrational spectroscopy experiments through vibrational frequency calculations.

Methods

The density functional theory calculations were done using the Vienna Ab initio Simulation Package (VASP). [37,38] The Perdew-Burke-Ernzerhof (PBE) functional was used with Hubbard U correction of 4.2 eV on Ti sites to adjust the incorrect description of Ti 3d orbitals.[39,40] The U value 4.2 eV was taken as it correctly depicts the electronic structure features observed experimentally with TiO_2, particularly the localized nature of electrons on surfaces with oxygen vacancies.[41] The dDsC dispersion correction was used to describe long-range van der Waals

interactions. [42–44] The electron kinetic energy cutoff is set at 500 eV. [45–47] The electronic energies and atomic forces were converged within 10^{-6} eV and 0.03 eV/A, respectively. The spurious dipole-dipole interaction between neighboring slabs in the z-direction was corrected using the Harris correction (Makov-Payne).[48]

The transition states were calculated using the Nudged Elastic Band Method using 8 images.

The adsorption energies/reaction pathway energies are calculated with equation 1:

$$E_{ads/intermediate} = E_{surf+DMMP} - E_{clean\ surface} - E_{Sarin(g)} \quad (1)$$

Computational Model

The 2x4 TiO_2(110) surface was cut from the bulk. The calculated bulk lattice constants using a gamma-centered k-points mesh of 4x4x4 are: a = 4.65 Å and c = 3.02 Å [49–51] The surface lattice vectors are: a = 13.16 Å and b = 12.07 Å (fig. S1). The surface consists of four O-Ti-O trilayers (12 atomic layers). A vacuum distance of 15 Å is set between slabs to avoid periodic interaction in the z-direction. The bottom-most three atomic layers are frozen to mimic the bulk. To model the defective surface, one oxygen atom in the bridging site (O_{2c}) was removed (fig. S2) as it was found to be the most stable vacancy site. [52–54] The removal of 1 O2c represents a vacancy site coverage of 0.125 ML, which agrees well with the experimentally observed vacancy coverage of r-TiO_2(110) crystals (between 0.08 to 0.15 ML)[55–57]. All surface calculations use the k-point mesh of 1x1x1. Literature and our test calculations[11] showed that using a k-points mesh of 3x3x1, larger surface or thicker surface models show no significant difference compared to our selected 2x4 surface calculated at the gamma point.[11]

Results

Pristine surface

The most stable sarin adsorption geometries on pristine TiO_2(110) from our DFT calculations can be seen in figure 2. Sarin adsorbs molecularly via the interaction between the O atom of the P=O group and a surface Ti cation (distance 2.09 Å) with an adsorption energy of -1.80 eV (Fig. 2A). An additional bond either between the oxygen of sarin's isopropoxy group and a surface Ti (2.60 Å) or fluorine with Ti (2.59 Å) further stabilizes the geometry with total adsorption energies

of -1.92 and -1.94 eV respectively (Fig. 2B and C). Finally, the adsorption geometry via the interactions of -F or -OC_3H_7 group with surface Ti atoms (with distances of 2.40 Å and 2.51 Å respectively) yields the weakest adsorption energy of -1.13 eV (Fig. 2D). Overall, our calculations showed that TiO_2(110) is an excellent trap for sarin due to the strong molecular binding. The adsorption energy of sarin is however significantly weaker than that of its simulant DMMP (by 0.41 eV).

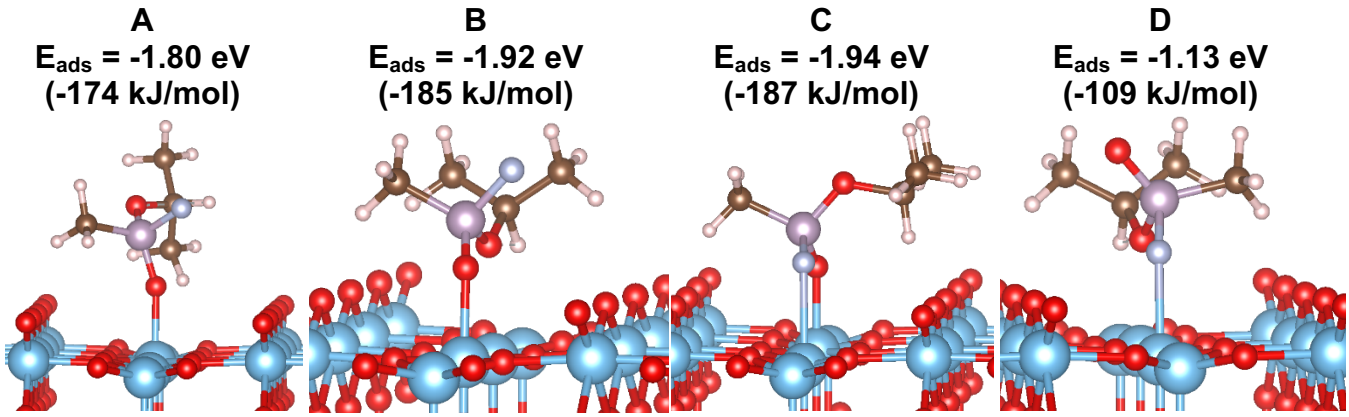

Figure 2 Molecular adsorption modes of sarin on TiO_2(110) with their adsorption energies.

From the molecularly adsorbed sarin, we have the option to cleave the P-F, P-OC_3H_7, or O-C_3H_7 bond. First, let us compare the decomposition initiated via the P-F and P-OC_3H_7 bond cleavages (fig. 3). The decomposition pathway initiated via the P-OC_3H_7 cleavage starts from geometry B of figure 2 and follows the B1-B3 pathway, whereas the pathway initiated via the P-F bond cleavage starts from geometry C of figure 2 and follows the C1-C2 pathway. Note that B1 is identical to B and C1 identical to C.

Calculations show that the cleavage of either the P-OC_3H_7 or the P-F bond has significantly high barriers, P-F being the least difficult bond to break (2.27 eV and 1.77 eV respectively). The P-OC_3H_7 bond cleavage transfers an isopropoxy towards a Ti_{5c} site and yields the B2 intermediate. B2 is more stable by 0.64 eV than the molecularly adsorbed sarin B1. On the other hand, the P-F bond cleavage to leave F on Ti_{5c} yields intermediate C2 which is 0.96 eV more stable than C1. A similar behavior persists for the second decomposition step (TS-B2 and TS-C2), where we can see that the P-F bond is easier to cleave than the P-OC_3H_7 bond, although both bond cleavages still have considerably high barriers (1.53 and 1.67 eV respectively). We conclude

that decomposition is unlikely to happen via the P-F or the P-OC_3H_7 bond cleavage on the pristine surface, unless at high temperature.

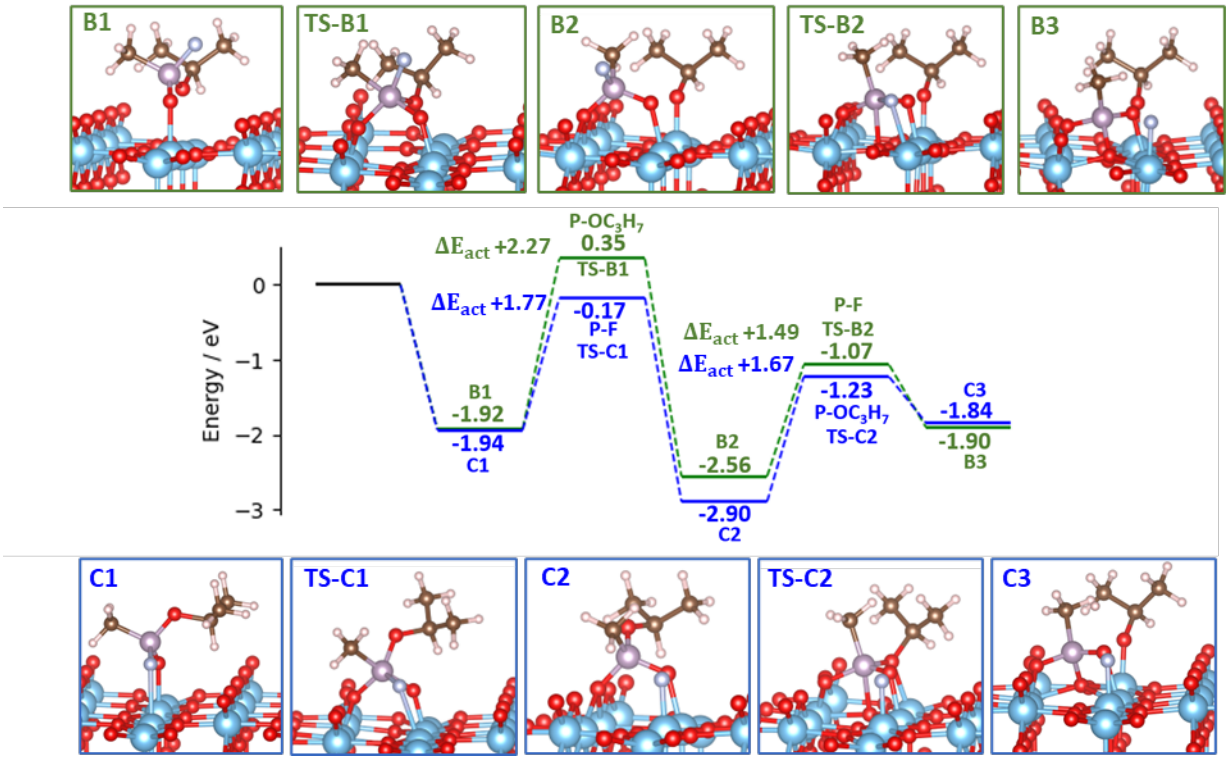

Figure 3 The energy profile of sarin decomposition on pristine r-TiO_2 via P-F and P-OC_3H_7 bond cleavage starting from the two most stable adsorption modes (adsorption modes B and C). The decomposition via P-OC_3H_7 cleavage is shown in the path B1-B3 whereas the P-F bond cleavage occurs along the path C1-C3. Elementary reaction barriers are indicated as ΔE_{act}.

On the other hand, decomposition via the O-C_3H_7 bond cleavage, transferring C_3H_7 towards a nearby O_{2c} is more likely (fig 4). The barrier for this step stood at 1.17 eV, rendering it a possible pathway at 455 K (see SI table S1). Further P-F bond cleavage as the second step also has a comparable low barrier of 1.00 eV. It is interesting to note that the removal of C_3H_7 reduces the barrier to cleave the P-F bond, compared to the case in figure 3. With such barriers, the thermal decomposition of sarin on pristine r-TiO_2 is possible at a high temperature (455K). However, the release of products such as HF and propene does not seem to be possible at low temperatures (fig. 4, intermediate C4*) as the barrier for C-H cleavage to form propene is 1.60 eV, which requires temperatures around ~610 K to overcome. Note that at any point during the

decomposition pathway, the P-containing intermediate may rearrange to a more stable configuration. We see such a case here where from C2* after O-C bond cleavage, the IMPA-like intermediate can rearrange first to an η_1 structure and be stabilized as an η_2 structure (C2* η_2), maximizing the P-O-Ti interactions. This rearrangement of the C2* intermediate competes with the P-F bond cleavage. We will now investigate the effect of O vacancies on the surface toward the barriers associated with either P-F, P-OC_3H_7, or O-C_3H_7 bond cleavage.

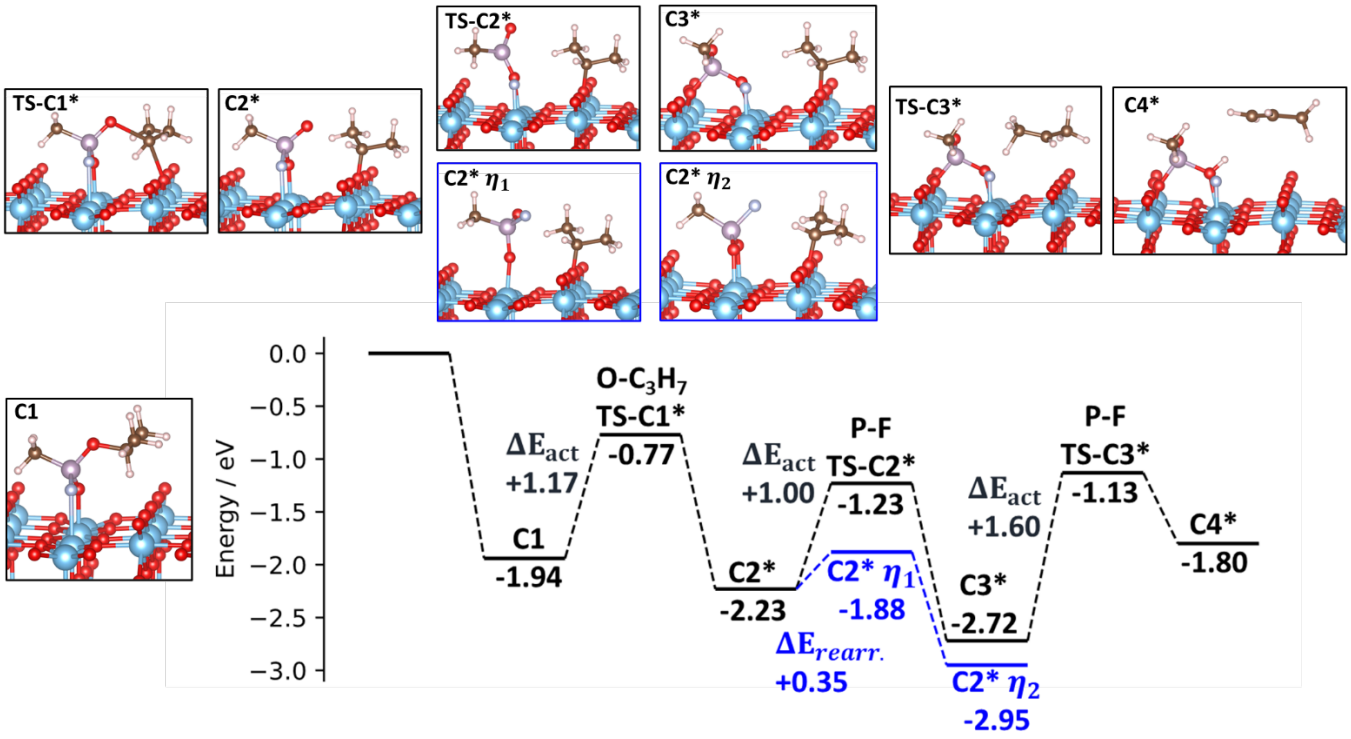

Figure 4. The energy profile of sarin decomposition on pristine r-TiO_2 via C-O bond cleavage starting from the two most stable adsorption modes C.

The effect of O vacancy

With the presence of an oxygen vacancy site, the most stable molecular sarin adsorption geometries involve the P=O group occupying the vacancy site (figure 5) with two possible isomers depending on which group interacts with Ti_{5c} (geometry E and F). In geometry E, in addition to P=O occupying the vacancy, there is a stabilizing interaction from a F-Ti_{5c} interaction. This geometry has an adsorption energy of -1.95 eV. Similarly, with geometry F, there is an additional interaction between the oxygen of the isopropoxy substituent and a surface Ti_{5c}, bringing the adsorption energy to -2.20 eV, which is the most stable configuration found. Further

sarin decomposition initiated via P-F and O-C bond cleavage may follow geometry E, whereas decomposition initiated with P-OR bond cleavage may follow geometry F.

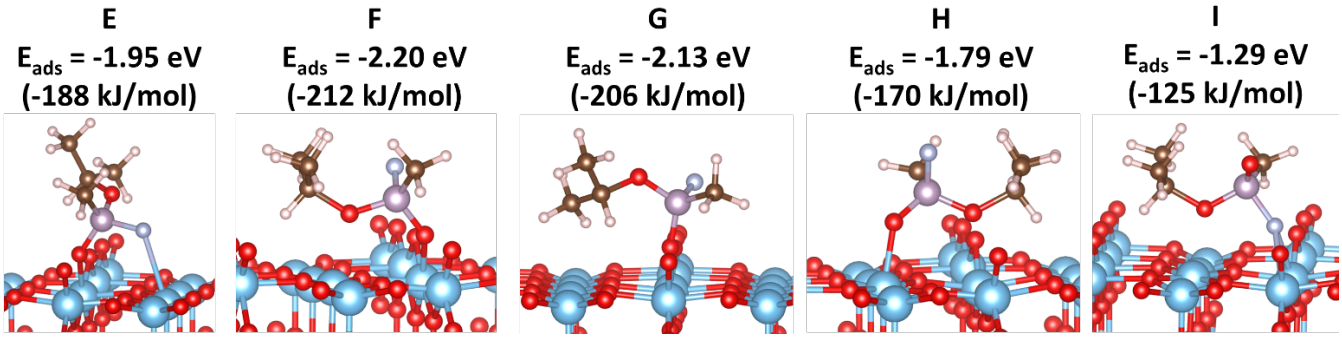

Figure 5 Sarin adsorption modes on the r-TiO_2 surface with an O vacancy.

Figure 6 shows the reaction pathway for O-C_3H_7 (E1-E2-E3) or P-F (E1-E4) bond cleavage starting from geometry E (E1=E). Since geometry F=F1 is more stable, it has also been included in the diagram, as the resting state of the molecule, and for the first step overall activation energies starting from F is indicated in the figure. The barrier to cleave the O-C_3H_7 bond from E1 is 1.4 eV (1.65 eV from F), which is higher than the case on the pristine surface (1.17 eV) and yields a stable intermediate E2 at -2.43 eV. Further P-F bond cleavage (E2-E3) as the second step is also exothermic by 0.35 eV (E3) with a barrier of 1.25 eV. Interestingly if we opt to first cleave the P-F bond (E1-E4), the barrier for this step is now greatly reduced from 1.77 eV (on the pristine surface) to only 0.85 eV from E1 (1.1 eV from F1). This process yields an intermediate E4 which is 0.79 eV more stable than the molecularly adsorbed sarin. Though further decomposition to cleave the P-OR bond from E4 is endothermic by 0.68 eV (not shown in figure 6), the intermediate may undergo C-H bond cleavage instead to produce gas phase propene. The barrier to release propene is 1.53 eV and the reaction is slightly exothermic by 0.16 eV (E4-E5). This pathway shows that the O vacancy defect facilitates the P-F bond cleavage and enables it at a temperature as low as 425 K, even if starting from the most stable structure F (compared to 675K on the pristine surface, see table S1 and S3 in the SI).

A similar barrier decrease can also be seen for the decomposition initiated with the P-OR bond cleavage from geometry F (fig. 7). Oxygen vacancies reduce the barrier to cleave the P-OR bond from 2.27 eV (pristine surface) to 1.05 eV (defective surface), and this cleavage can occur at

410K (table S3 in SI). The P-OC_3H_7 bond cleavage transition state shows a hexa-coordinated P atom, with an extra P-O bond involving a three-fold O atom on TiO_2, trans to the P-F bond. This additional P-O interaction stabilizes the transition state and is not present in the initial state F1 nor in the product state F2 of that elementary step. The following step to cleave the P-F bond remains relatively more facile in comparison to the case of pristine surface as well with a barrier of 1.01 eV.

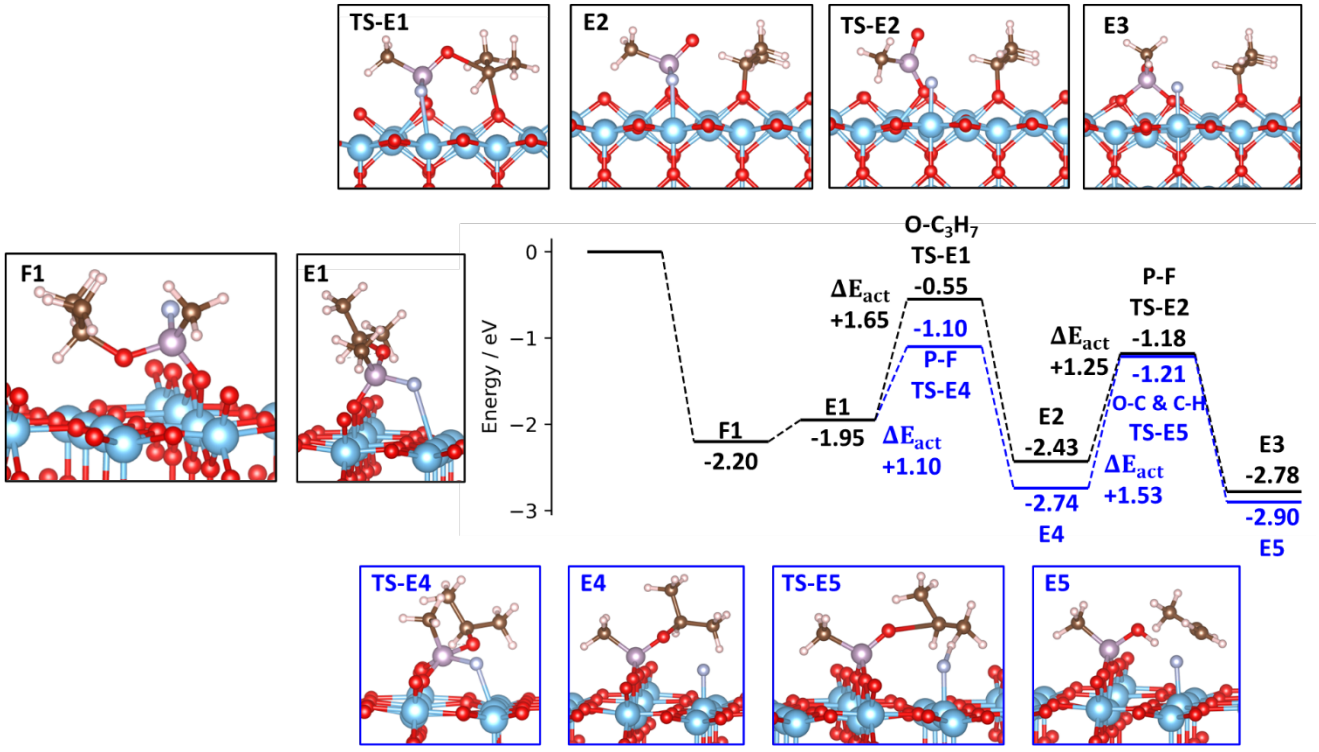

Figure 6 Sarin decomposition on the r-TiO_2 (110) surface with an O vacancy initiated via P-F (blue) or O-C (black) bond cleavage. The decomposition starts from Sarin's most stable adsorption mode (intermediate F here is written as F1, the numbering is to denote the step of the reaction). Activation energies for the first step are calculated from F1.

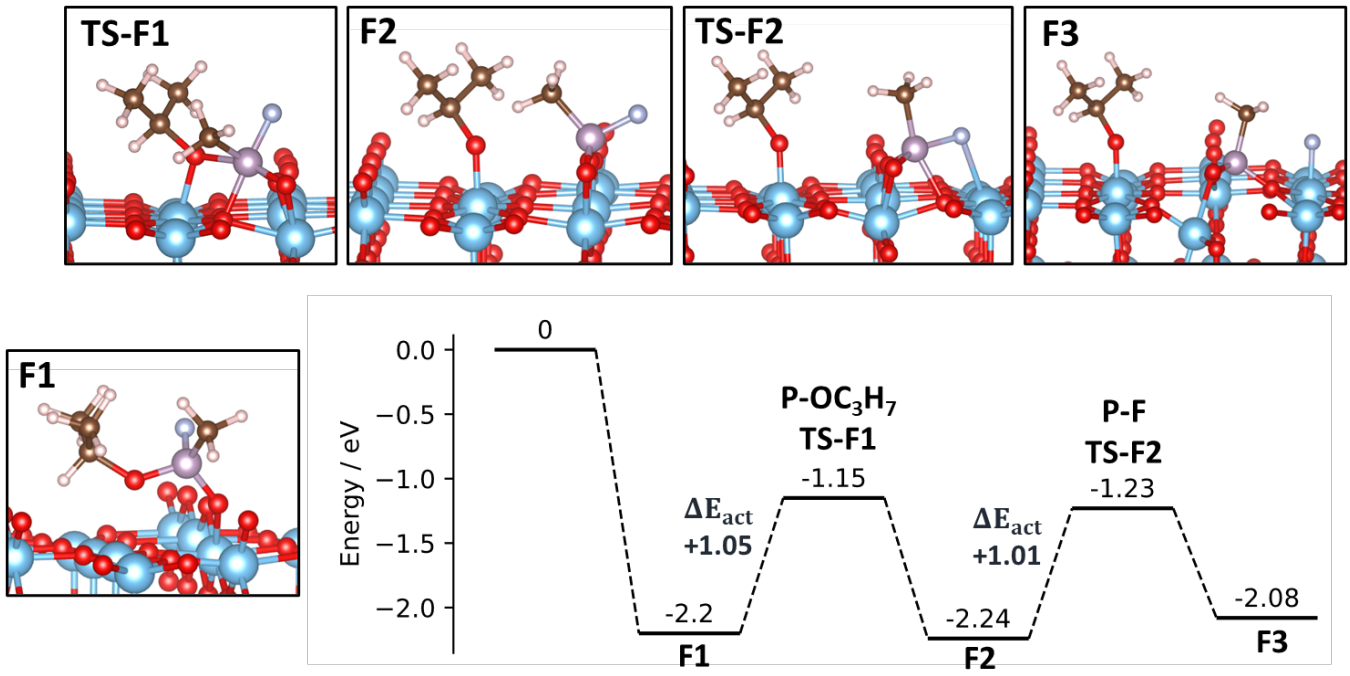

Figure 7 Sarin decomposition pathway on the r-TiO_2 (110) surface with an O vacancy initiated via P-OR (R= isopropyl) bond cleavage. The sarin initial adsorption geometry is structure F = F1.

Vibrational analysis

To strengthen the interaction with experimental observation on the nature of adsorbed sarin and decomposition intermediates, vibrational analysis calculations were performed on the molecularly adsorbed species and selected intermediates which are accessible at 500 K from our pathways (following previous experimental work by Tsyshevsky et.al.[29]). However, it is known that the PBE functional tends to underestimate frequencies in comparison to the experiment. A work by Le et al. comparing experimental and theoretical frequencies for sarin adsorbed intact on anatase TiO_2(101) suggested that PBE underestimates sarin characteristic modes by 60 cm-1 in comparison to experimental observation.[58] In order to better understand the intrinsic error on frequencies from our first principle calculations, IR frequencies for gas phase sarin were calculated with the DFT PBE-dDsC functional as a benchmark and compared with the experimental result (Table 1). In comparison to the experiment, PBE-dDsC underestimates IR frequencies by ~ 50 cm-1. This value is used here as a correction shift term

when comparing the frequencies of the molecularly adsorbed sarin and the intermediates obtained after thermal treatment.

Table 1 Experimental and calculated vibrational frequencies for gas phase sarin. Experimental data is from ref [29].

IR band assignment	GB vapor phase (exp.)	GB vapor phase (theory)	Δ
ν(P–O)	1303	1250	-53
ν(C–O–(P))	1020	978	-42
ν(P–F)	845	792	-53
δ(P–CH3)	1328	1285	-43

Table 2 shows the characteristic IR frequencies for molecularly adsorbed sarin prior to the thermal decomposition treatment. The four best geometries of molecularly adsorbed sarin were chosen to represent the ensemble of surface species (on the pristine surface, structures A, B, and C from Fig. 2, on the defective surface with O vacancies, structures E and F from Fig. 5). Corrected values (shown in parenthesis in table 2) show good agreement with experimental observation. The ensemble of frequencies observed experimentally in the range 1271-1200 cm^{-1} can be assigned to the P=O bond stretch, more or less weakened by the interaction with surface Ti (dative bond P=O-Ti) compared to the gas phase species. Such frequencies are seen for the chemisorption structures on the pristine surface, structures A, B, and C, wherein A sarin is interacting with the surface with only one P=O-Ti bond while in B and C, an additional P-OPr-Ti or P-F-Ti interaction is created. The modes associated with these frequencies are not purely located on the P-O bond but show small couplings with deformations on other ligands of P. For C, which is the most stable chemisorption structure, one mode is lowered to 1125 cm^{-1} and can be described as a P=O stretch, coupled with the O of the alkoxy ligand in a symmetric (O-P-O) stretch modes, which is seen in the experiment. Adsorption modes on defective surface E and F (P=O occupies an O vacancy with either F or O-Pr interacting with Ti) also show similar (O-P-O) stretch modes. Amongst all structures, these calculated (O-P-O) stretching modes at 1125-1173 cm-1 are slightly overestimated in comparison with the experimental peak assigned to (O-P-O) at 1090-1145. All sarin adsorption configurations possess the (C-O-(P)) stretch modes and the (P-CH3) seen experimentally, with significant weakening of the frequency for geometry B and F. Note that the experiment was performed on a powder P25 sample which contains a

mixture of anatase and rutile phase of titania. Vibrational modes on the anatase phase of the sample might differ somewhat and are not included in the calculation.

Table 2 IR band assignment comparison between sarin adsorption experiments at room temperature (ref [29])and theoretical frequencies for molecularly adsorbed sarin. Corrected frequencies are shown in parentheses. *Data is not included ref 29.

IR band assignment	**Molecularly adsorbed**					
	exp	theory (A)	theory (B)	theory (C)	theory (E)	theory (F)
v(P–O)	1271-1200	1180, 1190 (1230, 1240)	1171, 1167 (1221, 1217)	1159 (1209)		
ν_s(O–P–O)	1090			1075 (1125)		
ν_{as}(O–P–O)	1145				1116 (1156)	1123 (1173)
v(C–O–(P))	1038	1007 (1057)	921, 917 (971, 967)	998 (1048)	1033 (1083)	924 (974)
v(P–F)	*	836 (886)	836 (886)	727 (777)	819 (869)	845 (895)
δ(P–CH3)	1320	1298 (1348)	1296 (1346)	1299 (1349)	1291 (1341)	1293 (1341)

Table 3 shows the characteristic IR frequencies for decomposed sarin after thermal treatment. Experiment at 500 K shows a decrease of intensity for the modes in the region 1271-1200 cm^{-1}, an increase in the broad region 1200-900 cm^{-1}, mainly at 1145-1135 and 1095-1075 cm^{-1}, and a decrease at 1038 cm^{-1}. From the calculated reaction profiles, on the pristine surface, the most abundant decomposition intermediate should be C2*η_2 (Fig. 4), where the sarin O-C bond is cleaved, followed by a rearrangement to form two Ti-O-P interactions. Consistently with the experiment, no mode occurs in the 1271-1200 cm^{-1} region, while O-P-O stretching modes arise at 1114 and 1088 cm^{-1}, associated with the Ti-O-P-O-Ti linkage formed in C2*η_2. Since the O-C bond is cleaved, no mode occurs at 1038 cm^{-1} (where the C-O-(P) stretching mode of chemisorbed sarin was). The vacancy defects pose a challenge to IR spectroscopy because of their low concentration. The most abundant intermediate after decomposition on the defective surface should be the intermediate E4, following sarin P-F bond cleavage. The release of propene from this intermediate is not accessible at 500 K. This intermediate is similar to IMPA and has three P-O bonds, two with the surface (one of them corresponds to the filing of the vacancy by the oxo (P=O) of sarin), hence generating three modes. One of them occurs at 1132

cm-1, close the 1145-1135 cm-1 enhanced region in the experimental spectrum. The other two (1029, 1054 cm-1) are lower. The C-O-(P) stretch is present but it is shifted to 1073 cm^{-1}, which is close to the experimental IR band peak assigned to O-P-O stretching, hence compatible with the decrease in the experiment around 1038 cm^{-1}, initial value of the C-O-(P) stretch in intact chemisorbed sarin.

Table 3 IR band assignment comparison of decomposed sarin after heating to 500 K between the experiment and theory. A negative sign (-) indicates disappearing bands and a positive sign (+) indicates increasing bands.

IR band assignment	**Heated to 500 K**		
	exp	theory (C2*η_2)	theory (E4)
v(P–O)	1271-1200 (-)		
vs(O–P–O)	1095-1075 (+)	1038 (1088)	1082(1132)
vas(O–P–O)	1145-1135 (+)	1064 (1114)	994, 979 (1054, 1029)
v(C–O–(P))	1038 (-)		1023 (1073)
v(P–F)	*	821 (871)	
δ(P–CH3)	1310	1294 (1344)	1278 (1328)

Therefore, the calculated vibrational frequencies validate the surface species obtained with our total energy calculations, with an ensemble of sarin chemisorbed structures at low temperatures, and intermediates of decomposition from C-O or P-F bond cleavage after thermal treatment.

Discussion

The complete decomposition pathways of sarin on the pristine and defective surface of rutile TiO_2(110) have been investigated via DFT calculations. On the pristine surface, the most stable sarin adsorption geometries involve the dative P=O---Ti_{5c} bond, with an additional stabilizing interaction from either the isopropoxy or fluorine groups, with adsorption energies of -1.92 eV (-185 kJ/mol) or -1.94 eV (-187kJ/mol), respectively. Our results agree very well with the data for other rutile metal oxides. The adsorption of sarin has previously been theoretically studied on MoO_2(110) where the most stable structure found is identical to that of structure C (P=O-Ti and

F-Ti binding modes) in figure 2, with a stronger adsorption energy of -229 kJ/mol.[26] The differences in adsorption energies may be attributed to the difference in surface cation acidity between titania and molybdenum. Additionally, our result agrees well with the work of Quintero et al. on rutile TiO_2 (sarin adsorption of -178 kJ/mol vs -187 kJ/mol). A slight difference may be attributed to the difference in dispersion correction employed.[28]

On the pristine surface, the cleavage of the P-OC_3H_7 or P-F bond of sarin was found to have high barriers (2.27 eV and 1.77 eV respectively). This behavior has been observed as well on DMMP, where the cleavage of a P-OCH_3 bond requires overcoming a barrier higher than 2 eV.[11] On the pristine surface, the P-F bond of sarin is less difficult to cleave compared to the P-OC_3H_7 bond, but still, the barrier is large. On the defective surface, both barriers to cleave the P-OC_3H_7 or P-F bond are considerably lowered and they become similar in magnitude. The barriers calculated with respect to the most stable isomer F1 of sarin are 1.1 and 1.05 eV, for the P-F and P-OC_3H_7 bond cleavage respectively. These bonds can therefore be broken on defective TiO_2 at moderate temperature (~425 K).

Calculations of vibrational frequencies of chemisorbed species and intermediates enable the validation of the dominant species proposed by the DFT reaction profiles and the interpretation of the experimental spectra in details. Two main results arise. First, Intact chemisorbed sarin configurations can introduce new O-P-O stretching frequencies, compared to the gas phase spectrum, seen in the room temperature experiment at 1145 and 1090 cm^{-1}. This is especially the case for the most stable configuration C. When interpreting their room temperature experimental spectrum, Tsyshevsky et al. interpreted the two new IR modes (1145 and 1090 cm^{-1}) as arising from decomposition products of sarin via P-F or P- O(Pr) bond cleavage (Pr stands for the isopropoxy moiety). Our vibrational calculations provide an alternative interpretation as intact chemisorbed sarin can explain the features at 1145 and 1090 cm^{-1} which is consistent with DFT calculations (ours and those from Tsyshevsky et al.) which show a sizeable barrier (>1eV) for decomposition which cannot be passed at room temperature.

Second, our vibrational analysis showed that dissociated sarin formed after temperature treatment reinforces the occurrence of frequencies at 1145 and 1090 cm^{-1} while decreasing modes in the higher range of 1200-1271 cm-1. In the presence of oxygen vacancies, unavoidable on rutile titania in UHV conditions, decomposition at moderate temperature (~425

K) can involve P-F or P-OC_3H_7 bond cleavages. The barriers are very similar for these two pathways, but P-F bond cleavage is more exothermic so products from P-F bond cleavage should dominate on the surface (intermediate E4). O-C bond cleavage is favored on the pristine surface, and afterward, the remaining surface intermediate may rearrange to a more stable adsorption geometry. Such a rearrangement is very accessible as the barrier is very low (+0.35 eV) and the reaction is quite exothermic (fig, 4 C2* to C2*η_2 ΔE = -0.72 eV). If the intermediate adopts the C2*η_2 conformation, further decomposition is unlikely. Our frequency calculations show that both the formation of C2*η_2 and E4 agree with the experimental spectra where Tsyshevsky et.al observe the disappearance of 1200-1271 cm-1 and an increase of intensity around 1145 and 1090 cm^{-1} frequencies.

Table 4: Barrier comparison of the first step of sarin decomposition via P-O, P-F, and O-C bond cleavage on pristine and defective surface

Bond cleaved	Pristine surface (activation T in K)	Defective surface (activation T in K)
P-OC_3H_7	2.27 eV (>800 K)	1.05 eV (~410 K)
P-F	1.77 eV (~675 K)	1.10 eV (~425 K)
O-C_3H_7	1.17 eV (~455 K)	1.39 eV (~535 K)

Upon decomposition, the P-containing intermediate persists on the surface, as P coordinates itself with surface oxygens. Gas products such as propene may arise from the alkoxy resulting from the decomposition via C-H bond cleavage. However, the barrier to cleave C-H is very high and both P-containing intermediates and alkoxy may poison the surface over time. The phenomenon of surface passivation for sarin is expected and has been before observed on DMMP and DIMP on titania and other metal oxides experimentally such as cupric, manganese, alumina, and iron oxides. [8,11,59–61]

It is also interesting to note that F- is stable on Ti sites. An experimental (FTIR) work by Hirakawa et.al. suggests that the formation of F-Ti species is favorable on fully hydrated powder titania in which all the Ti sites are occupied with water and proton molecules. Upon F- ion injection towards a hydrated titania surface, Hirakawa et al. observed v(OH) and δ(H_2O) shift, which indicates that either the dissociated water molecules (Ti-OH and proton on O_2c) or molecular H_2O on Ti sites are substituted by F- ions.[30] Our calculations agree well, as we see large stabilization of the

intermediates in steps involving the formation of Ti-F species on the surface, compared to the intermediates which involve the formation of Ti-OC_3H_7. On a defective surface, P-F bond cleavage and subsequent Ti-F and P-containing (similar to IMPA) surface intermediate formation are exothermic by 0.79 eV. The P-F bond cleavage renders the following P-OC_3H_7 bond cleavage difficult, which is in agreement with the experimental observation reporting the presence of IMPA-like surface fragments.[29,30]

Our results shed light on the question of whether DMMP is a good enough simulant for sarin decomposition reactivity. The decomposition profiles of sarin and its simulant DMMP show similarities but also key differences. Similarities are: (1) strong adsorption of both molecules which involves the dative P=O---Ti5c bond, (2) difficult P-OR/P-F bond cleavage on the pristine surface, the O-C bond being the easiest to cleave on the pristine surface, and (3) the decrease of the barrier for P-OR (or equivalently P-F) bond cleavage in the presence of O vacancies. The key difference between sarin and DMMP chemistries lies in the presence of the P-F bond itself in sarin and not in DMMP. The P-F bond cleavage is significantly less difficult than the P-OR bond cleavage on the pristine surface. Additionally, the Ti-F formation upon P-F bond cleavage is much more favorable than the Ti-OC_3H_7 formation. As a consequence, there is a pathway initiated by P-F bond cleavage for sarin, which is absent for DMMP. The most obvious difference is in the case of the O vacancy containing TiO_2(110) surface with a first decomposition step of sarin by P-F bond cleavage possible at 425 K (with much higher exothermicity), while the reactivity of DMMP starts at 600K by P-OR or O-C cleavage.[11] The F substituent also has an influence in facilitating the P-OR bond cleavage of sarin in the presence of the O vacancy, the energy barrier being 1.05 eV for sarin versus 1.4 eV for DMMP. An additional bond between P and surface O atoms is created in the transition state for P-OC_3H_7 bond cleavage of sarin: the electronegative F ligand positively polarizes P, which is more prone to interact with surface O atoms.

Therefore, DMMP is not an accurate simulant of sarin for chemical reactivity since sarin is significantly more reactive for decomposition than DMMP.

Conclusion

In conclusion, our analysis shows that the reactivity of sarin on pristine rutile titania is low, despite the strong adsorption energy, and that decomposition most likely initiates via the O-C bond cleavage (barrier 1.17 eV) while P-OR (R= C_3H_7 isopropyl) or P-F cleavage is highly activated (barriers larger than 2 eV). In contrast on the defective rutile surface containing O vacancies, a first decomposition step by P-OR or P-F cleavage can occur at moderate temperature (~425K), with a barrier of ~1.1 eV. The transition state for the P-OR bond cleavage is stabilized by an additional interaction between P and surface O, facilitated by the electronic effect of the F ligand. These relatively easy initial decomposition paths for sarin on rutile TiO_2 in the presence of O vacancies are in sharp contrast with the reactivity of the less toxic simulant DMMP, for which the decomposition only initiates at 600K on the same O vacancy-containing model surface. The formation of the Ti-F bond stabilizes the system significantly which gives thermodynamic preference towards the P-F bond cleavage. The produced surface IMPA-like intermediate is unlikely to undergo further decomposition via P-OC_3H_7 bond cleavage. It may react to produce propene, but the reaction is significantly activated and requires a higher temperature (585 K). Frequency calculation indicates that intact molecular adsorption of sarin can explain the experimental spectrum at room temperature, while further decomposition by C-O or P-F bond cleavage, presumably at O vacancies, is responsible for the spectral evolution seen at 500K, in agreement with calculated barriers. This theoretical work, therefore, reconciles theory and experiments for the sarin decomposition pathway on TiO_2 surfaces, proposes a pathway for initial moderate temperature decomposition by P-F or P-OC_3H_7 cleavage on O vacancies, and demonstrates the limited accuracy of DMMP as a reactivity simulant for sarin.

Acknowledgments

We acknowledge the support of this work by the US Army under Program No W911NF-21-1-0361. This work used the Extreme Science and Engineering Discovery Environment (XSEDE), which is supported by the National Science Foundation grant number ACI-1548562. This work used computational and storage services associated with the Hoffman2 Shared Cluster provided by UCLA Institute for Digital Research and Education's Research Technology Group.

Supporting Information

Surface model used and calculated reaction rate constants for each step of all decomposition reaction pathways.

References

(1) Yanagisawa, N. The Nerve Agent Sarin: History, Clinical Manifestations, and Treatment. *Brain Nerve* **2014**, *66* (5), 561–569.

(2) Tušek, D.; Ašperger, D.; Bačić, I.; Ćurković, L.; Macan, J. Environmentally Acceptable Sorbents of Chemical Warfare Agent Simulants. *J Mater Sci* **2017**, *52* (5), 2591–2604.

(3) Aliha, H. M.; Khodadadi, A. A.; Mortazavi, Y. The Sensing Behaviour of Metal Oxides (ZnO, CuO and Sm2O3) Doped-SnO2 for Detection of Low Concentrations of Chlorinated Volatile Organic Compounds. *Sens Actuators B Chem* **2013**, *181*, 637–643.

(4) Oh, S. W.; Kim, Y. H.; Yoo, D. J.; Oh, S. M.; Park, S. J. Sensing Behaviour of Semconducting Metal Oxides for the Detection of Organophosphorus Compounds. *Sens Actuators B Chem* **1993**, *13* (1–3), 400–403.

(5) Mitchell, M. B.; Sheinker, V. N.; Mintz, E. A. Adsorption and Decomposition of Dimethyl Methylphosphonate on Metal Oxides. *J Phys Chem B* **1997**, *101* (51), 11192–11203. https://doi.org/10.1021/jp972724b.

(6) Chen, D. A.; Ratliff, J. S.; Hu, X.; Gordon, W. O.; Senanayake, S. D.; Mullins, D. R. Dimethyl Methylphosphonate Decomposition on Fully Oxidized and Partially Reduced Ceria Thin Films. *Surf Sci* **2010**, *604* (5–6), 574–587. https://doi.org/10.1016/j.susc.2009.12.028.

(7) Mitchell, M. B.; Sheinker, V. N.; Tesfamichael, A. B.; Gatimu, E. N.; Nunley, M. Decomposition of Dimethyl Methylphosphonate (DMMP) on Supported Cerium and Iron Co-Impregnated Oxides at Room Temperature. *J Phys Chem B* **2003**, *107* (2), 580–586.

(8) Walenta, C.; Xu, F.; Tesvara, C.; O'Connor, C.; Sautet, P.; Friend, C. Facile Decomposition of Organophosphonates by Dual Lewis Sites on a Fe_3O_4(111) Film. *The Journal of Physical Chemistry C 124* (23), 12432–12441. https://doi.org/10.1021/acs.jpcc.0c01708.

(9) Templeton, M. K.; Weinberg, W. H. Adsorption and Decomposition of Dimethyl Methylphosphonate on an Aluminum Oxide Surface. *J Am Chem Soc* **1985**, *107* (1), 97–108.

(10) Mitchell, M. B.; Sheinker, V. N.; Cox, W. W.; Gatimu, E. N.; Tesfamichael, A. B. The Room Temperature Decomposition Mechanism of Dimethyl Methylphosphonate (DMMP) on Alumina-Supported Cerium Oxide− Participation of Nano-Sized Cerium Oxide Domains. *J Phys Chem B* **2004**, *108* (5), 1634–1645.

(11) Tesvara, C.; Walenta, C.; Sautet, P. Oxidative Decomposition of Dimethyl Methylphosphonate on Rutile TiO 2 (110): The Role of Oxygen Vacancies. *Physical Chemistry Chemical Physics* **2022**, *24* (38), 23402–23419.

(12) Housaindokht, M. R.; Zamand, N. A DFT Study of Associative and Dissociative Chemical Adsorption of DMMP onto SnO2 (110) Surface Nano-Cluster. *Struct Chem* **2015**, *26* (1), 87–96.

(13) Biswas, S.; Wong, B. M. High-Temperature Decomposition of Diisopropyl Methylphosphonate on Alumina: Mechanistic Predictions from Ab Initio Molecular Dynamics. *The Journal of Physical Chemistry C* **2021**, *125* (40), 21922–21932. https://doi.org/10.1021/acs.jpcc.1c05632.

(14) Zhou, J.; Varazo, K.; Reddic, J. E.; Myrick, M. L.; Chen, D. A. Decomposition of Dimethyl Methylphosphonate on TiO2(110): Principal Component Analysis Applied to X-Ray Photoelectron Spectroscopy. *Anal Chim Acta* **2003**, *496* (1–2), 289–300. https://doi.org/10.1016/S0003-2670(03)01008-0.

(15) Rusu, C. N.; Yates, J. T. Adsorption and Decomposition of Dimethyl Methylphosphonate on TiO 2. *J Phys Chem B* **2000**, *104* (51), 12292–12298. https://doi.org/10.1021/jp002560q.

(16) Panayotov, D. A.; Morris, J. R. Thermal Decomposition of a Chemical Warfare Agent Simulant (DMMP) on TiO 2 : Adsorbate Reactions with Lattice Oxygen as Studied by Infrared Spectroscopy. *The Journal of Physical Chemistry C* **2009**, *113* (35), 15684–15691. https://doi.org/10.1021/jp9036233.

(17) Panayotov, D. A.; Morris, J. R. Uptake of a Chemical Warfare Agent Simulant (DMMP) on TiO 2 : Reactive Adsorption and Active Site Poisoning. *Langmuir* **2009**, *25* (6), 3652–3658. https://doi.org/10.1021/la804018b.

(18) Panayotov, D. A.; Morris, J. R. Catalytic Degradation of a Chemical Warfare Agent Simulant: Reaction Mechanisms on TiO2-Supported Au Nanoparticles. *The Journal of Physical Chemistry C* **2008**, *112* (19), 7496–7502. https://doi.org/10.1021/jp7118668.

(19) Holdren, S.; Tsyshevsky, R.; Fears, K.; Owrutsky, J.; Wu, T.; Wang, X.; Eichhorn, B. W.; Kuklja, M. M.; Zachariah, M. R. Adsorption and Destruction of the G-Series Nerve Agent Simulant Dimethyl Methylphosphonate on Zinc Oxide. *ACS Catal* **2019**, *9* (2), 902–911. https://doi.org/10.1021/acscatal.8b02999.

(20) Schweigert, I. v.; Gunlycke, D. Hydrolysis of Dimethyl Methylphosphonate by the Cyclic Tetramer of Zirconium Hydroxide. *Journal of Physical Chemistry A* **2017**, *121* (40). https://doi.org/10.1021/acs.jpca.7b06403.

(21) Troya, D. Reaction Mechanism of Nerve-Agent Decomposition with Zr-Based Metal Organic Frameworks. *Journal of Physical Chemistry C* **2016**, *120* (51). https://doi.org/10.1021/acs.jpcc.6b10530.

(22) Plonka, A. M.; Wang, Q.; Gordon, W. O.; Balboa, A.; Troya, D.; Guo, W.; Sharp, C. H.; Senanayake, S. D.; Morris, J. R.; Hill, C. L.; Frenkel, A. I. In Situ Probes of Capture and Decomposition of Chemical Warfare Agent Simulants by Zr-Based Metal Organic Frameworks. *J Am Chem Soc* **2017**, *139* (2), 599–602. https://doi.org/10.1021/jacs.6b11373.

(23) Wang, G.; Sharp, C.; Plonka, A. M.; Wang, Q.; Frenkel, A. I.; Guo, W.; Hill, C.; Smith, C.; Kollar, J.; Troya, D.; Morris, J. R. Mechanism and Kinetics for Reaction of the Chemical Warfare Agent Simulant, DMMP(g), with Zirconium(IV) MOFs: An Ultrahigh-Vacuum and DFT Study. *The Journal of Physical Chemistry C* **2017**, *121* (21), 11261–11272. https://doi.org/10.1021/acs.jpcc.7b00070.

(24) Vasudevan, A.; Senyurt, E. I.; Schoenitz, M.; Dreizin, E. L. Removal of Diisopropyl Methyl Phosphonate (DIMP) from Heated Metal Oxide Surfaces. *J Hazard Mater* **2023**, *443*, 130154. https://doi.org/https://doi.org/10.1016/j.jhazmat.2022.130154.

(25) Michalkova, A.; Ilchenko, M.; Gorb, L.; Leszczynski, J. Theoretical Study of the Adsorption and Decomposition of Sarin on Magnesium Oxide. *Journal of Physical Chemistry B* **2004**, *108* (17). https://doi.org/10.1021/jp036766d.

(26) Tsyshevsky, R.; Head, A. R.; Trotochaud, L.; Bluhm, H.; Kuklja, M. M. Mechanisms of Degradation of Toxic Nerve Agents: Quantum-Chemical Insight into Interactions of Sarin and Soman with Molybdenum Dioxide. *Surf Sci* **2020**, *700*. https://doi.org/10.1016/j.susc.2020.121639.

(27) Tsyshevsky, R.; Holdren, S.; Eichhorn, B. W.; Zachariah, M. R.; Kuklja, M. M. Sarin Decomposition on Pristine and Hydroxylated ZnO: Quantum-Chemical Modeling. *Journal of Physical Chemistry C* **2019**, *123* (43). https://doi.org/10.1021/acs.jpcc.9b07974.

(28) Quintero, Y. C.; Nagarajan, R. Molecular and Dissociative Adsorption of DMMP, Sarin and Soman on Dry and Wet TiO2(110) Using Density Functional Theory. *Surf Sci* **2018**, *675*, 26–35. https://doi.org/https://doi.org/10.1016/j.susc.2018.04.002.

(29) Tsyshevsky, R.; McEntee, M.; Durke, E. M.; Karwacki, C.; Kuklja, M. M. Degradation of Fatal Toxic Nerve Agents on Dry TiO2. *ACS Appl Mater Interfaces* **2021**, *13* (1), 696–705. https://doi.org/10.1021/acsami.0c19261.

(30) Hirakawa, T.; Sato, K.; Komano, A.; Kishi, S.; K. Nishimoto, C.; Mera, N.; Kugishima, M.; Sano, T.; Ichinose, H.; Negishi, N.; Seto, Y.; Takeuchi, K. Experimental Study on Adsorption and Photocatalytic Decomposition of Isopropyl Methylphosphonofluoridate at Surface of TiO2 Photocatalyst. *The Journal of Physical Chemistry C* **2010**, *114* (5), 2305–2314. https://doi.org/10.1021/jp910911x.

(31) Kuiper, A. E. T.; van Bokhoven, J. J. G. M.; Medema, J. The Role of Heterogeneity in the Kinetics of a Surface Reaction: I. Infrared Characterization of the Adsorption Structures of Organophosphonates and Their Decomposition. *J Catal* **1976**, *43* (1), 154–167. https://doi.org/https://doi.org/10.1016/0021-9517(76)90302-X.

(32) Bermudez, V. M. Computational Study of the Adsorption of Dimethyl Methylphosphonate (DMMP) on the (010) Surface of Anatase TiO2 with and without Faceting. *Surf Sci* **2010**, *604* (7), 706–712. https://doi.org/https://doi.org/10.1016/j.susc.2010.01.021.

(33) Bermudez, V. M. First-Principles Study of Adsorption of Dimethyl Methylphosphonate on the TiO2 Anatase (001) Surface: Formation of a Stable Titanyl (Ti═O) Site. *The Journal of Physical Chemistry C* **2011**, *115* (14), 6741–6747. https://doi.org/10.1021/jp200009s.

(34) Bermudez, V. M. Ab Initio Study of the Interaction of Dimethyl Methylphosphonate with Rutile (110) and Anatase (101) TiO2 Surfaces. *The Journal of Physical Chemistry C* **2010**, *114* (7), 3063–3074.

(35) Zhou, J.; Ma, S.; Kang, Y. C.; Chen, D. A. Dimethyl Methylphosphonate Decomposition on Titania-Supported Ni Clusters and Films: A Comparison of Chemical Activity on Different Ni Surfaces. *J Phys Chem B* **2004**, *108* (31), 11633–11644. https://doi.org/10.1021/jp040185m.

(36) Trubitsyn, D. A.; Vorontsov, A. v. Molecular and Reactive Adsorption of Dimethyl Methylphosphonate over (0 0 1) and (1 0 0) Anatase Clusters. *Comput Theor Chem* **2013**, *1020*, 63–71.

(37) Kresse, G.; Furthmüller, J. Software VASP, Vienna (1999). *Phys. Rev. B* **1996**, *54* (11), 169.

(38) Kresse, G.; Furthmüller, J. Efficiency of Ab-Initio Total Energy Calculations for Metals and Semiconductors Using a Plane-Wave Basis Set. *Comput Mater Sci* **1996**, *6* (1), 15–50. https://doi.org/https://doi.org/10.1016/0927-0256(96)00008-0.

(39) Anisimov, V. I.; Aryasetiawan, F.; Lichtenstein, A. I. First-Principles Calculations of the Electronic Structure and Spectra of Strongly Correlated Systems: The **LDA** + *U* Method. *Journal of Physics: Condensed Matter* **1997**, *9* (4), 767–808. https://doi.org/10.1088/0953-8984/9/4/002.

(40) Dudarev, S. L.; Botton, G. A.; Savrasov, S. Y.; Humphreys, C. J.; Sutton, A. P. Electron-Energy-Loss Spectra and the Structural Stability of Nickel Oxide: An LSDA+U Study. *Phys Rev B* **1998**, *57* (3), 1505–1509. https://doi.org/10.1103/PhysRevB.57.1505.

(41) Morgan, B. J.; Watson, G. W. A DFT+U Description of Oxygen Vacancies at the TiO2 Rutile (110) Surface. *Surf Sci* **2007**, *601* (21), 5034–5041. https://doi.org/https://doi.org/10.1016/j.susc.2007.08.025.

(42) Steinmann, S. N.; Corminboeuf, C. Comprehensive Benchmarking of a Density-Dependent Dispersion Correction. *J Chem Theory Comput* **2011**, *7* (11), 3567–3577. https://doi.org/10.1021/ct200602x.

(43) Steinmann, S. N.; Corminboeuf, C. A Generalized-Gradient Approximation Exchange Hole Model for Dispersion Coefficients. *J Chem Phys* **2011**, *134* (4), 044117. https://doi.org/10.1063/1.3545985.

(44) Perdew, J. P.; Burke, K.; Ernzerhof, M. Generalized Gradient Approximation Made Simple. *Phys Rev Lett* **1996**, *77* (18), 3865–3868. https://doi.org/10.1103/PhysRevLett.77.3865.

(45) Kresse, G.; Joubert, D. From Ultrasoft Pseudopotentials to the Projector Augmented-Wave Method. *Phys Rev B* **1999**, *59* (3), 1758–1775. https://doi.org/10.1103/PhysRevB.59.1758.

(46) Kresse, G.; Furthmüller, J. Efficient Iterative Schemes for Ab Initio Total-Energy Calculations Using a Plane-Wave Basis Set. *Phys Rev B* **1996**, *54* (16), 11169–11186. https://doi.org/10.1103/PhysRevB.54.11169.

(47) Blöchl, P. E. Projector Augmented-Wave Method. *Phys Rev B* **1994**, *50* (24), 17953–17979. https://doi.org/10.1103/PhysRevB.50.17953.

(48) Makov, G.; Payne, M. C. Periodic Boundary Conditions in Ab Initio Calculations. *Phys Rev B* **1995**, *51* (7), 4014–4022. https://doi.org/10.1103/PhysRevB.51.4014.

(49) Tang, Y.; Asokan, C.; Xu, M.; Graham, G. W.; Pan, X.; Christopher, P.; Li, J.; Sautet, P. Rh Single Atoms on TiO2 Dynamically Respond to Reaction Conditions by Adapting Their Site. *Nat Commun* **2019**, *10* (1), 1–18. https://doi.org/10.1038/s41467-019-12461-6.

(50) Yu, Y.-Y.; Gong, X.-Q. CO Oxidation at Rutile TiO2(110): Role of Oxygen Vacancies and Titanium Interstitials. *ACS Catal* **2015**, *5* (4), 2042–2050. https://doi.org/10.1021/cs501900q.

(51) Deskins, N. A.; Rousseau, R.; Dupuis, M. Distribution of Ti3+ Surface Sites in Reduced TiO2. *The Journal of Physical Chemistry C* **2011**, *115* (15), 7562–7572. https://doi.org/10.1021/jp2001139.

(52) Li, H.; Guo, Y.; Robertson, J. Calculation of TiO2 Surface and Subsurface Oxygen Vacancy by the Screened Exchange Functional. *The Journal of Physical Chemistry C* **2015**, *119* (32), 18160–18166. https://doi.org/10.1021/acs.jpcc.5b02430.

(53) Pacchioni, G. Oxygen Vacancy: The Invisible Agent on Oxide Surfaces. *ChemPhysChem* **2003**, *4* (10), 1041–1047.

(54) Sánchez-Sánchez, C.; González, C.; Jelinek, P.; Méndez, J.; de Andres, P. L.; Martín-Gago, J. A.; López, M. F. Understanding Atomic-Resolved STM Images on TiO_2 (110)-(1 × 1) Surface by DFT Calculations. *Nanotechnology* **2010**, *21* (40), 405702. https://doi.org/10.1088/0957-4484/21/40/405702.

(55) di Valentin, C.; Pacchioni, G.; Selloni, A. Electronic Structure of Defect States in Hydroxylated and Reduced Rutile ${\mathrm{TiO}}_{2}(110)$ Surfaces. *Phys Rev Lett* **2006**, *97* (16), 166803. https://doi.org/10.1103/PhysRevLett.97.166803.

(56) Schaub, R.; Wahlström, E.; Rønnau, A.; Lægsgaard, E.; Stensgaard, I.; Besenbacher, F. Oxygen-Mediated Diffusion of Oxygen Vacancies on the TiO2(110) Surface. *Science (1979)* **2003**, *299* (5605), 377–379. https://doi.org/10.1126/science.1078962.

(57) Henderson, M. A.; Otero-Tapia, S.; Castro, M. E. The Chemistry of Methanol on the TiO 2 (110) Surface: The Influence of Vacancies and Coadsorbed Species. *Faraday Discuss* **1999**, *114*, 313–329.

(58) Le, N. Q.; Bazargan, G.; Schweigert, I. v; Gunlycke, D. Vibrational Signatures of Sarin Adsorption on Anatase Surfaces. *Surf Sci* **2021**, *705*, 121765.

(59) Wang, L.; Denchy, M.; Blando, N.; Hansen, L.; Bilik, B.; Tang, X.; Hicks, Z.; Bowen, K. H. Thermal Decomposition of Dimethyl Methylphosphonate on Size-Selected Clusters: A Comparative Study between Copper Metal and Cupric Oxide Clusters. *The Journal of Physical Chemistry C* **2021**, *125* (21), 11348–11358. https://doi.org/10.1021/acs.jpcc.1c00952.

(60) Segal, S. R.; Cao, L.; Suib, S. L.; Tang, X.; Satyapal, S. Thermal Decomposition of Dimethyl Methylphosphonate over Manganese Oxide Catalysts. *J Catal* **2001**, *198* (1), 66–76.

(61) Mukhopadhyay, S.; Schoenitz, M.; Dreizin, E. L. Vapor-Phase Decomposition of Dimethyl Methylphosphonate (DMMP), a Sarin Surrogate, in Presence of Metal Oxides. *Defence Technology* **2021**, *17* (4), 1095–1114. https://doi.org/https://doi.org/10.1016/j.dt.2020.08.010.

TOC graphics